Observation and analysis of lower-hybrid-current-drive density limit in EAST

M.H. Li [a], S.G. Baek [b], G.M. Wallace [b], B.J. Ding [a*], C.B. Wu [a], G.H. Yan [a], P.T. Bonoli [b], M. Wang [a*], L. Liu [a], L.M. Zhao [a], Z.G. Wu [a], H. Yang [a], S.Y. Lin [a], Q. Zang [a], N. Yan [a], H.L. Zhao [a], J. Huang [a], X.M. Zhai [a], X.X. Li [c], X.J. Zhang [a] and X.Z. Gong [a]

[a]*Institute of Plasma Physics, Chinese Academy of Sciences, Hefei 230031, P. R. China*

[b]*MIT Plasma Science and Fusion Center, Cambridge, MA 02139, USA*

[c]*Department of Nuclear Physics, University of South China, Hengyang 421001, P. R. China*

∗E-mail: bjding@ipp.ac.cn and mwang@ipp.ac.cn

Abstract

Lower hybrid current drive (LHCD) experiments with line-averaged density up to ~ $5.1 \times 10^{19}/m^3$ were performed in EAST L-mode plasmas. When the line-averaged density rises above a critical value, the hard X-ray (HXR) emission fall to the noise level, indicating that the LHCD density limit is encountered. The experimental results show that the LHCD density limit can be increased with higher wave source frequency (f_0) and higher magnetic field (B_t). Although a higher LHCD density limit is obtained by a higher magnetic field for both 2.45 GHz and 4.6 GHz waves, the results show a stronger dependence on the magnetic field for the 4.6 GHz case. Analysis suggests that, for the normal operation with relatively low magnetic field (1.6 T ≤ B_t ≤ 2.5T) on EAST, the dominant mechanisms responsible for the LHCD density limit are different between the 2.45 GHz and 4.6 GHz waves. The wave accessibility plays a more significant role during 4.6 GHz LHCD experiments, while parasitic losses due to parametric decay instability (PDIs) dominate the accessibility issue in the 2.45 GHz case. Collisional loss in the scrape-off layer (SOL) may explain the 4.6 GHz result when combined with the accessibility limit at high density and low temperature.

1. Introduction

Lower hybrid current drive (LHCD), characterized by the highest current drive efficiency with respect to other auxiliary heating and current drive (CD) methods, has

been successfully used in present tokamaks. Since its start in the early 1980s [1, 2], significant progress has been achieved in long-pulse steady-state operation. Fully non-inductive plasma discharges of up to 3.6 MA on JT-60U [3] and 3 MA on JET [4] have been obtained with LHCD. A plasma current of 0.5 MA has been sustained with LHCD in a steady-state regime for up to 6 min on Tore-Supra [5]. Recently on EAST, a long-pulse H-mode scenario over 100 s with a current fraction of LHCD ~ 75% [6], and a stationary I-mode plasma with a world-record pulse length of 1056 s sustained by LHCD and electron cyclotron resonance heating (ECRH) [7] have been realized. LHCD is expected to be the most efficient tool for driving off-axis current in ITER advanced scenarios and is under consideration for heating and CD upgrades [8, 9]. However, nearly every experiment to date [10-12] shows that LHCD efficiency decreases with electron density more strongly than the theoretical expectation which scales with the inverse of density. Furthermore, some experiments encountered a "density limit" problem, namely, the current-drive effects disappear above a critical density [13, 14]. In order to obtain more complete physical and numerical models which can be used with increased confidence to assess LHCD at high density for extrapolation to ITER advanced scenarios, a joint ITPA (International Tokamak Physics Activity) activity of systematic multi-machine investigations was carried out including Alcator C-Mod, Tore Supra, FTU and EAST devices [15]. Many extremely valuable results have been obtained. For example, Alcator C-Mod [16] and Tore Supra [17] experiments indicate that collisional absorption in the scrape-off layer (SOL) and wave scattering from fluctuations are important loss mechanisms respectively. Extension of density limit was demonstrated on FTU [18] and Alcator C-Mod [19] by using lithiation and at a lower Greenwald fraction at the same line-averaged density $<n_e>$, both favorable for reducing the wave-plasma interactions at the plasma edge. Previous investigations on EAST [20 - 22] show that lithiation and higher wave frequency can help to improve CD efficiency, but the line-averaged density coverage in the past LHCD experiment is limited to the range of $<n_e> < 3.5 \times 10^{19}/m^3$; namely, the experiments did not reach the LHCD density limit for 4.6 GHz wave. New experiments are performed to investigate the LHCD density limit at high density,

extending the line-averaged density to 5.1 × 10^{19} m^{-3}. Here the density limit is the critical density at which the hard X-ray (HXR) count rate falls to the noise floor. Recent scenario developments on EAST are focused at high density to demonstrate reactor-relevant plasma β [23, 24]. In this density regime, both wave accessibility and edge non-linear effects need to be considered.

This paper compares the LHCD efficiency at higher density with different wave source frequencies (f_0) and magnetic field (B_t). The dominant mechanisms responsible for the 2.45 GHz and 4.6 GHz LHCD density limits are investigated. The organization of this paper is as follows. The experimental set-up is shown in Section 2. Section 3 describes the experimental observation of density limit on EAST with 2.45 GHz and 4.6 GHz waves respectively. An analysis of the potential mechanisms responsible for the anomalous loss of LHCD efficiency is given in section 4. Finally, we summarize the paper in section 5.

2. Experimental set-up

Experimental Advanced Superconducting Tokamak (EAST) is a fully superconducting tokamak with an ITER-like divertor configuration and its main feature is steady-state long-pulse operation. It is a medium-sized tokamak with a major radius of 1.89 m, and a minor radius of 0.45 m. There are two high-power LHCD systems on EAST with different operating frequencies (2.45 GHz /4 MW [25] and 4.6 GHz /6 MW [26]). LH power is coupled to the plasma using a Fully-Active-Multijunction (FAM) launcher for both systems (see Fig. 1). The whole launcher for 2.45 GHz is arranged in an array of 5 rows and 4 columns fed by 20 klystrons, each capable of delivering 200kW for 1000 s, while for 4.6 GHz, it is arranged in an array of 12 rows and 6 columns fed by 24 klystrons (i.e., one klystron corresponds to 3 rows × 1 column), each capable of delivering 250 kW for 1000 s. The total size of the launchers is 0.736 m in height × 0.472 m in width and 0.776 m × 0.442 m, respectively for 2.45 GHz and 4.6 GHz waves. For both launchers, the power directivity, defined as power ratio in negative parallel refractive index ($N_{||}$) to the total radiated power can be as high as 76%, and the reflection coefficient less than 1% around the optimum density [27].

A 20-chord poloidally viewing HXR diagnostic measures the fast electron bremsstrahlung emission. A detector with a 2 mm aluminum vacuum window measures the HXR energy of 20 - 300 keV every 1 ms. The HXR count rate is taken as a proxy for the density of the fast electrons generated by LHCD.

There are two radio frequency (RF) probes located outside the EAST vacuum vessel for measuring the LH wave signals. The detected RF signals are then sent to two frequency spectrum analyzers with a frequency resolution of 30 kHz every 20 ms during LH power injection. These two probes are far from the LH antennas in order to guarantee that the RF signals are detected after the interaction of the waves with the plasma, rather than from LH antennas directly. The RF probe spectrum consists of RF power reflected back outside from the machine. The detected signal qualitatively documents the nature of LH power interaction with the plasma. This diagnostic technique was used for monitoring wave-plasma edge interactions, such as the parametric decay instability (PDIs) of LH waves in LHCD experiments on many tokamaks [28 - 30].

All the eight discharges analyzed in this paper are performed in L-mode deuterium plasmas with upper single null (USN) divertor configuration. In order to reach the LHCD density limit, the plasma density was ramped throughout each discharge. The launched power spectra are shown in Fig. 2. The peak $N_{\parallel}$ of the first main lobe is 2.1 and 2.04 for 2.45 GHz and 4.6 GHz LH waves, respectively. The spectral width of the first main lobe ($\Delta N_{\parallel}$) is 0.5 (2.45 GHz) and 0.3 (4.6 GHz). The narrower spectral width for the 4.6 GHz wave is due to the larger number of sub-waveguides in one row and a higher source frequency (i.e., $\Delta N_{\parallel} \propto 1 / (n{\cdot}f)$ with n the number of sub-waveguides). The coupled LH power is about 1.0 MW for both 2.45 GHz and 4.6 GHz LHCD experiments with the same plasma current of 400 kA and four toroidal magnetic field values on the magnetic axis (B_t = 1.6 T, 1.8 T, 2.25 T, and 2.5 T).

3. Experimental results

Figure 3 shows the time evolution of several key plasma parameters during a typical ramped density discharge with 2.45 GHz LHCD. The line-averaged plasma density $<n_e>$ was increased from 1.3 to 4.2 × 10^{19}/m^3 gradually during the plasma current

plateau by feed-back control with supersonic molecular beam injection (SMBI). The LH power was injected when the plasma current reached the flat top. Although the coupling was not good at the beginning due to the relatively low density, the injected power kept nearly constant when density increased to $2.5 \times 10^{19}/m^3$. The line integrated x-ray emission on the central chords (from 8 to 20) was decreased during density ramp up and dropped to the noise level when density increased to $3.5 \times 10^{19}/m^3$, indicating reaching the LHCD density limit. At the same time, the non-thermal ECE temperature at the plasma edge ($\rho \sim 1$) decreases to a level that is in agreement with the Thomson scattering measurement (several 10's of eV), suggesting the fast electron population generated by LH waves disappeared.

Figure 4 shows the line-integrated HXR emission as a function of the line-averaged density with different LH wave frequencies (f_0 = 2.45 GHz and 4.6 GHz) and magnetic fields (B_t = 1.6T, 1.8 T, 2.25 T, and 2.5 T). The HXR count rates fall as density rises, and then above a critical density, the count rates fall to the noise level, indicating that the LHCD density limit occurs. By comparing the variation of HXR emission with the plasma density, we can find that for a given source frequency at a higher magnetic field, the CD efficiency and LHCD density limit are increased gradually. Meanwhile, there is a clear frequency dependence during our experiments; namely, for a given magnetic field, the HXR data in the 2.45 GHz case shows that its level is always lower than that for the 4.6 GHz. Consequently, higher source frequency and higher magnetic field are beneficial to increasing both LHCD density limit and CD efficiency. Note that the density range for the case of 2.45 GHz with B_t = 1.8 T (#93292) is very small. Here we use a power-law fitting to evaluate the density limit. This conclusion can also be drawn from comparing the residual loop voltage (V_{loop}) with different magnetic field and LH wave frequencies, as shown in Fig. 5. A lower residual loop voltage is observed in higher source frequency or higher magnetic field cases.

The dependence of density limit (n_{e_limit}) on wave frequencies and magnetic fields is plotted in Fig. 6. We can see that the LHCD density limit for 4.6 GHz wave is higher by a factor of 1.2 - 1.5 than the 2.45 GHz wave. A dependency of density limit

on wave frequency, $n_{e_limit} \propto f_0^{0.45}$, is found in one machine with the same plasma conditions. Similar results were also observed on Versator II tokamak, but with lower plasma parameters ($<n_e> < 2.5 \times 10^{19}/m^3$) and lower LH power ($P_{LH} < 100$ kW) [31]. Besides, the LHCD density limit during 4.6 GHz experiments show stronger dependence on the magnetic field than that of 2.45 GHz.

4. Analysis of the observed different LHCD density limit

The purpose of this section is to analyze the observed LHCD density limit given in section 3 and hence to look for potential mechanisms for the anomalous loss of LHCD efficiency at high density.

4.1 Wave accessibility

The LH wave accessibility condition given by [32, 33]

$$N_{||}^{\mathrm{acc}} = \frac{\omega_{\mathrm{pe}}}{\omega_{\mathrm{ce}}} + \sqrt{1 + (\frac{\omega_{\mathrm{pe}}}{\omega_{\mathrm{ce}}})^2 - (\frac{\omega_{\mathrm{pi}}}{\omega})^2} \qquad (1),$$

is recognized to play an important role for LHCD experiments, where ω_{pe} is the local electron plasma frequency, ω_{ce} the local electron cyclotron frequency, ω_{pi} the local ion plasma frequency and ω the wave frequency respectively. This condition determines the maximum wave phase velocity parallel to the magnetic field in the main plasma. LH waves with $N_{||} < N_{||}^{acc}$ will be mode converted to the fast wave at that layer of $N_{||} = N_{||}^{acc}$ and reflected back to the plasma edge. The role of LH wave accessibility in enabling or preventing the LHCD effect has not been assessed on EAST thus far. Indeed, from one side, as the LH accessibility condition was no more satisfied, a marked drop of LHCD efficiency was observed in FTU [12]. A large radiation loss was generated in JT-60U, which is a possible consequence of enhanced plasma-wall interaction by inaccessible LH waves [34]. On the other side, the lacking of LHCD effects occurred at a relatively high plasma density in the experiments in JET, independently of the validity of the accessibility condition [14].

According to the Eq. (1), LH wave accessibility is improved by increasing the magnetic field, which can explain the higher CD efficiency at higher magnetic field observed on EAST at a fixed source frequency. A dependence of LHCD efficiency on the magnetic field was also found in Alcator C Tokamak [28]. However, the

accessibility effects cannot explain the difference between 2.45 GHz and 4.6 GHz LHCD experiments, because for a given $N_{||}$ value, the wave accessibility is worse for a higher frequency wave.

It is important to note that the toroidal effects can shift the parallel refractive index upward or downward [35]. In this paper, the role of wave accessibility in 2.45 GHz and 4.6 GHz LHCD experiments at high density is studied by using a ray-tracing code GENRAY [36], which takes account of the toroidal effects. The wave propagation is calculated from the cold plasma dispersion relation [35]. The collision damping with a simple scrape-off layer (SOL) model ~ exp ($-r/\lambda$) is considered, where r is the distance from the last closed flux surface (LCFS), and λ is the decay length. The density and temperature profiles in the main plasma region are shown in Fig. 7, which are measured by Thomson scattering at the time points coinciding with the LHCD density limit. Only the first main lobe of the power spectrum is considered (see Fig. 2) and for this lobe we calculate 13 rays with $N_{||}$ varies from $N_{||peak} - \Delta N_{||} / 2$ to $N_{||peak} + \Delta N_{||} / 2$. Modeling and simulations show that the evolution of $N_{||}$ along the ray trajectories depends on the poloidal launching position [35, 37]. In our simulations, 5 poloidal locations and 4 poloidal locations are considered for 2.45 GHz and 4.6 GHz waves respectively, corresponding to waveguide arrays of the LH antennas.

Figures 8(a) and (b) show the simulated ray trajectories in a poloidal cross-section at 2.45 GHz and 4.6 GHz with B_t = 2.5 T, respectively. All the rays at 2.45 GHz can penetrate into the plasma interior even during the first pass. Due to the relatively low electron temperature, only a small amount of the launched power is absorbed during the first few passes. On the other hand, the rays at 4.6 GHz cannot penetrate into the inner region and travel around the plasma periphery during the first few passes. Figures 9(a) and (b) illustrate the variation of $N_{||}$, the local accessibility criterion ($N_{||}^{acc}$), and the normalized radius (ρ) as a function of the poloidal length of ray trajectory with different poloidal locations. The initial $N_{||}$ are 2.1 and 2.04, respectively for 2.45 GHz and 4.6 GHz waves, corresponding to the peak $N_{||}$ value of the first main spectral lobe. It is seen that the accessibility is well guaranteed for the 2.45 GHz wave before the power fully is absorbed when the rays undergo a large $N_{||}$

upshift. For 4.6 GHz, the rays initially propagate inward until they reach the accessibility layer ($N_{||} = N_{||}^{acc}$) where a mode conversion from the slow wave to the fast wave, and back to the slow wave at the slow-wave cut-off layer in the plasma periphery. These rays experience many reflections between the mode conversion layer ($\rho > 0.8$) and the edge density cutoff layer. As a consequence, the power loss in the SOL due to the electron-ion collision (P_{cl}) is high as ~ 65% (see Fig.10). However, for the 2.45 GHz case with the LHCD density limit of $3.5 \times 10^{19}/m^3$, the collisional loss fraction is only 32%. These results indicate that accessibility plays a significant role in 4.6 GHz LHCD experiments at high density, while it is not an issue for 2.45 GHz case.

The output of GENRAY is passed to the bounce averaged Fokker-Planck solver CQL3D [38] to calculate the bremsstrahlung emission, which can be compared with the experimental HXR results. Fig. 10 shows the measured and simulated bremsstrahlung emission versus different line-averaged densities. The simulations use experimental profiles of plasma density and temperature, and effective charge number (Z_{eff}). It is seen that the modeling reproduces the decline of the HXR counts at a high density for the 4.6 GHz case. For 2.45 GHz case, the simulated bremsstrahlung emission at high density is higher than the experimental data by a factor of ~ 3. The modeling results also show a higher collisional power loss for the 2.45 GHz than the 4.6 GHz wave with comparable density. This is because that the rays with lower frequency have a more extended excursion outside the LCFS, and secondly, the collision damping rate is inversely proportional to the square of source frequency [17, 39].

4.2 Parametric decay instabilities

Parametric decay instabilities (PDIs) are a non-linear interaction between RF waves and edge plasma [40, 41], which have been observed in many LH experiments such as FTU [18], Alcator C-Mod [42] and Tore Supra [43]. As the parametrically excited sideband waves, which lead to a power depletion of pump waves, are expected to have a substantially higher value of $N_{||}$ than the pump wave, the current drive efficiency will be reduced significantly. According to the theory [44], the PDI ion

cyclotron growth rate is inversely proportional to the squared ratio ω_0/ω_{LH}, where $\omega_{LH} \approx \omega_{pi} / (1 + \omega^2_{pe} / \omega^2_{ce})^{1/2}$, is the lower hybrid frequency. A correlation between the LHCD density limit and the parameter ω_0/ω_{LH} was found in Alcator C tokamak [11]. For the case of B_t = 2.5 T, the value of ω_0/ω_{LH} is estimated to be ~ 3.2 (5.5) for 2.45 GHz (4.6 GHz) waves when reaching the LHCD density limits of $3.5 \times 10^{19}/m^3$ ($5.1 \times 10^{19}/m^3$), where the frequency ω_{LH} is evaluated at the center of the plasma. Accordingly, a stronger PDI process is foreseen with 2.45 GHz waves than 4.6 GHz.

4.2.1 Measurements of the frequency spectrum

The frequency spectra measured at two different densities are shown in Figures 11(a) and (b), respectively for 2.45 GHz and 4.6 GHz waves. It is seen that the spectral broadening of the pump waves represented by the pump width is similar in the low-density case for both LH waves. Here, the pump width Δf_P is defined as the full width 20 dB below the maximum. When the density increased to 3.5×10^{19}/m3, the observed pump broadening of 2.45 GHz waves is more severe than 4.6 GHz, i.e. the pump width of 2.45 GHz is almost double that of 4.6 GHz. In theory, a modification of the launched $N_{||}$ spectrum will occur simultaneously in the same process of producing a frequency broadening [45], leading to a degradation of CD efficiency. Correlation between the degradation of CD efficiency and the frequency broadening was observed during the ASDEX experiments [46].

In addition to more significant pump broadening, we observed an ion cyclotron sideband down-shifted by approximately 15 MHz from the operating frequency at 2.45 GHz. The strength of the ion cyclotron sideband (P_1 ~ -35.5 dBm) is about 16% of the pump waves (P_0 ~ -27.8 dBm). Given that the width of the sideband is much wider than that of the pump wave, the frequency-integrated spectral power of the sideband waves are comparable to that of the pump. The peak amplitude of the pump wave is observed to decrease by a factor of 8 when the density increases from 2.2 to 3.5×10^{19}/m3. For 4.6 GHz case, it is only reduced by a factor of 4 and there is no sideband detected.

Figures 12(a) and (b) plot the frequency-integrated spectral power of the pump waves (with ± 2 MHz around the operating line frequency) and the first down-shifted

sideband (with ± 2 MHz around the peak) as a function of line-averaged density, respectively for 2.45 GHz and 4.6 GHz waves. The integrated spectral power of the pump waves, which drive current effectively, is lowered by ~ 67% when density increases to 3.5×10^{19}/m3, and the ratio of the side-band waves to the pump reach up to ~ 35 % for 2.45 GHz. As mentioned above, since these side-band LH waves have much high $N_{||}$, this power transferred from the pump is expected to be deposited in the edge region with a negligible CD efficiency. These results suggest that the PDI effects could be the main mechanism responsible for the observed loss of CD efficiency for 2.45 GHz. On the other hand, it is difficult to link the degradation of the CD efficiency to the power depletion of pump waves at around 4.6 GHz, because the pump power at the LHCD density limit still remains about 73 % (compared to the low-density case). Note that we do not directly compare the measured spectral power between 2.45 GHz and 4.6 GHz cases, because neither the sensitivity of the RF probes to LH waves at around 2.45 GHz and 4.6 GHz nor the transmission loss is exactly the same.

4.2.2 PDI modeling and analysis

A PDI modeling with the parametric dispersion code, MP-PDI, described in [11, 40, 47] is utilized to calculate the PDI driven mode growth rate with two assumed edge densities $n_{e_edge} = 0.25 \times 10^{19}$ m^{-3}, 0.5×10^{19} m^{-3}. In the modelling, other parameters are as follows: $P_{LH} = 1.0$ MW, $L_z = 73.6$ cm (77.6 cm for 4.6 GHz) and $L_y = 47.2$ cm (44.2 cm for 4.6 GHz), deuterium plasma, $T_{e_edge} = T_{i_edge} = 25$ eV, $B_t = 1.83$ T, $N_{//0} = 2$, and the ion mode at $N_{//} = 6$, where P_{LH} is the LH power, L_z and L_z is the dimension of the LH antenna in the toroidal and poloidal direction, respectively. The density and temperature parameters assumed in this calculation correspond to the nominal SOL values in EAST. The perpendicular wavenumber of the lower sideband is assumed to be normal to the perpendicular wavenumber of the pump wave. The modeling results are shown in Fig. 13, where γ is the mode growth rate, ω_R is real part of the mode frequency, and ω_{ci} is the local ion cyclotron frequency. It is seen that the growth rates of ion sound quasi-modes (ω_R / ω_{ci} ~ 0.2) increase with increasing density in the 2.45 GHz case, whereas very small variation in the peak growth rate of the ion sound

quasi-mode is observed in the 4.6 GHz case. The above calculations are qualitatively in agreement with the measurement that the frequency spectrum is less broadened in the 4.6 GHz case than in the 2.45 GHz. In addition, at high density, the normalized peak growth rates of the ion cyclotron quasi-mode ($\omega_R / \omega_{ci} \sim 1$) in the 4.6 GHz case become nearly half of that in the 2.45 GHz case. Such results indicate a stronger ion cyclotron PDI behavior at high density with a 2.45 GHz LH wave, consistent with the measured spectrum. The convective growth or the saturation mechanism are not considered in this model.

5. Summary and conclusions

LHCD experiments with different magnetic fields were performed at high density for 2.45 GHz and 4.6 GHz waves, respectively. We observed that when the density increased above a critical density, the current-drive effects indicated by the HXR emission disappeared. By raising the source frequency from 2.45 GHz to 4.6 GHz, the LHCD density limit has been increased by a factor of 1.2 - 1.5. The HXR production rates improve with a higher magnetic field for both LH waves, but the experiments show a stronger magnetic field dependence of the LHCD density limit for a 4.6 GHz wave than 2.45 GHz. These observations are in line with our past results reported in [20 - 22], but we extended the density regime and conducted magnetic field scan in this paper.

Wave accessibility studies have been performed for the first time in high-density plasmas on EAST, using a ray-tracing code GENRAY which includes toroidal wave propagation effects. Simulations show that when reaching the LHCD density limit, the 4.6 GHz waves mainly propagate around the plasma periphery during the first few passes and cannot penetrate the plasma interior, while for the 2.45 GHz case, the accessibility condition is well satisfied on the first pass. Ray tracing / Fokker-Planck models of GENRAY/CQL3D, which includes collisional damping effects, can reproduce the decline of the HXR counts at a high density for the 4.6 GHz case. On the contrary, the modeling results show a large discrepancy with the experimental data for 2.45 GHz LHCD at high density.

The spectral measurements indicate that the PDI behavior in the 2.45 GHz case is

much stronger than that in the 4.6 GHz case at high density. Larger spectral broadening of the pump wave at 2.45 GHz is observed, accompanied by an ion cyclotron sideband with power comparable to the pump wave, documenting the stronger occurrence of non-linear decay of the pump wave. The integrated spectral power of the pump wave is decreased to ~ 33% above a critical density, while for 4.6 GHz, the pump power still remains to be about 73 %. PDI calculations show that the growth rates of the ion cyclotron quasi-mode in the 2.45 GHz case are almost double that in the 4.6 GHz case, which is consistent qualitatively with the experimental measurements.

In conclusion, the results presented in this paper indicate that, on EAST when operates with the magnetic field in the range of 1.6 T ≤ B_t ≤ 2.5T, wave accessibility is the dominant mechanism for the 4.6 GHz LHCD density limit, and for the 2.45 GHz case, parasitic losses due to PDIs dominate the wave accessibility. In order to enhance the CD capability, the 2.45 GHz system will be replaced by a new 4.6 GHz / 4 MW system with a passive - active - multijunction (PAM) launcher, which can solve the PDIs issue. The accessibility issue at 4.6 GHz could be mitigated by raising the magnetic field. For example, the LHCD density limit can be increased to ~ 7.6×10^{19} m^{-3} when the magnetic field is upgraded to 3.5 T, according to the scaling ($n_{e_limit} \propto B_t^{1.0}$) found in this work. In this case, the ratio ω_0 / ω_{LH} is still as high as 4.1. A rough assessment of wave accessibility and PDIs (indicated by the value of ω_0 / ω_{LH}) for ITER (steady-state, inductive and hybrid) scenarios and CFETR hybrid scenario is illustrated in Fig. 14 (red stars). The parameters for ITER scenarios are: $\omega_0 = 2\pi \times 5.0$ GHz, B_t = 5.3 T, n_{e0} = 7.3 (steady-state), 10.2 (inductive), 8.6 (hybrid) $\times 10^{19}/m^3$ [48]. The parameters for CFETR hybrid scenario are: $\omega_0 = 2\pi \times 4.6$ GHz, $n_{e0}=12 \times 10^{19}/m^3$, and B_t = 6.5 T [49]. The accessibility condition can be satisfied with $N_{\|}$ = 1.8 for both ITER and CFETR scenarios. If we adopt the results of Alcator C tokamak, ω_0 / $\omega_{LH} \approx$ 2 as a threshold value for the plasma condition of PDIs excitation, the source frequency of 4.6 GHz on CFETR, corresponding to ω_0 / ω_{LH} ~ 3.2, is acceptable. On ITER with 5.0 GHz LH waves, it has a great margin of operation for all scenarios since ω_0 / ω_{LH} > 4.0.

It is worth pointing out that the regime under investigation in this paper is an L-mode plasma, which is different from the high performance H-mode plasmas for a reactor scenario. The temperature will be much higher in the high β plasmas. Next work will study the LHCD characters in high density and high β plasmas.

Acknowledgmentsk

This work is supported by the National Natural Science Foundation of China (Grant Nos. 11775259, 11975266, 11805233 and 11975276), the Comprehensive Research Facility for Fusion Technology Program of China under Contract No. 2018-000052-73-01-001228, Anhui Provincial Natural Science Foundation No. 2008085J04, and an International Collaboration Grant No. DE-SC0010492 from the US Department of Energy.

References

[1] Yamamoto T. et al 1980 Phys. Rev. Lett. 45 716.

[2] Bernabei S. et al 1982 Phys. Rev. Lett. 49 1255.

[3] Naito O. and the JT-60 Team 1993 Plasma Phys. Control. Fusion 35 B215.

[4] JET Team 1994 in Plasma Physics and Controlled Nuclear Fusion Research (Proc. 15th Int. Conf. Seville, 1994), Vol. 1, IAEA, Vienna (1995) 423.

[5] Houtte D. van et al 2004 Nucl. Fusion 44 L11.

[6] Gong X.Z. et al 2019 Nucl. Fusion 59 086030.

[7] Song Y.T. et al 2022, Realization of Thousand-Second Improved Confinement Plasma with Super I-Mode in Tokamak EAST, Science Advances (under review).

[8] Bibet Ph. et al 2005 Fusion Eng. Des. 74 419.

[9] Hoang G.T. et al 2009 Nucl. Fusion 49 075001.

[10] Fisch N.J. and Boozer A. H. 1980 Phys. Rev. Lett. 45 720.

[11] Takase Y. et al 1985 Phys. Fluids 28 983.

[12] Pericoli-Ridolfini V. et al 1999 Phys. Rev. Lett. 82 93.

[13] Luckhardt S.C. et al 1982 Phys. Rev. Lett. 48 152.

[14] Cesario R. et al 2011 Plasma Phys. Control. Fusion 53 085011.

[15] Ding B.J. et al 2018 Nucl. Fusion 58 095003.

[16] Wallace G.M. et al 2010 Phys. Plasmas 17 082508.

[17] Goniche M. et al 2010 Plasma Phys. Control. Fusion 52 124031.

[18] Cesario R. et al 2010 Nature Commun. 1 55.

[19] Baek S.G. et al 2018 Phys. Rev. Lett. 121 055001.

[20] Ding B.J. et al 2018 Nucl. Fusion 58 126015.

[21] Li M.H. et al 2019 Plasma Phys. Control. Fusion 61 065005.

[22] Baek S.G. et al 2021 Nuclear Materials and Energy 26 100955.

[23] Huang J. et al 2020 Plasma Phys. Control. Fusion 62 014019.

[24] Zhai X.M. et al 2022 Nucl. Fusion 62 076015.

[25] Shan J.F. et al, A New 4 MW LHCD System for EAST, in Proceedings of the 23rd IAEA Fusion Energy Conference, Daejon, Korea (2010).

[26] Liu F.K. et al 2016 Fusion Engineering and Design 113 131.

[27] Li M.H. et al 2020 AIP Conference Proceedings 2254 080005.

[28] Porkolab M. et al 1984 Phys. Rev. Lett. 53 450.

[29] Cesario R. et al 1992 Nucl. Fusion 32 2127.

[30] Pericoli-Ridolfini V. et al 1992 Nucl. Fusion 32 286.

[31] Mayberry M.J. et al 1985 Phys. Rev. Lett. 55 829.

[32] Stix T.H., The Theory of Plasma Waves (McGraw-Hill, New York, 1962).

[33] Golant V.E. 1972 Sov. Phys. - Tech. Phys. 16 1980.

[34] Ikeda Y. et al 1994 Nucl. Fusion 34 871.

[35] Bonoli P. T. and Englade R. C. 1986 Phys. Fluids 29 2937.

[36] Smirnov A. P. and Harvey R. 1995 Bull. Am. Phys. Soc. 40 1837.

[37] Peysson Y. et al 2016 Plasma Phys. Control. Fusion 58 044008.

[38] Harvey R. W. and McCoy M. in Proceedings of the IAEA Technical Committee Meeting on Simulation and Modeling of Thermonuclear Plasmas, Montreal, 1992, International Atomic Energy Agency, Vienna, 1992, pp. 489-526.

[39] Barbato E. Nucl. Fusion 51 (2011) 103032.

[40] Porkolab M. et al 1977 Phys. Rev. Lett. 38 230.

[41] Liu C. S. and Tripathi V. K. 1986 Phys. Rep. 130 143.

[42] Baek S.G. et al 2013 Plasma Phys. Controlled Fusion 55 052001.

[43] Goniche M. et al 2013 Nucl. Fusion 53 033010.

[44] Porkolab M. 1977 Phys. Fluid 20 2058.

[45] Takase Y. et al 1984 Phys. Rev. Lett. 53 274.

[46] Pericoli-Ridolfini V. et al 1994 Nucl. Fusion 34 469.

[47] Baek S.G. et al 2014 Phys. Plasmas 21 061511.

[48] Decker J. et al 2011 Nucl. Fusion 51 073025.

[49] Wallace G.M. et al 2021 Nucl. Fusion 61 106009.

Captions

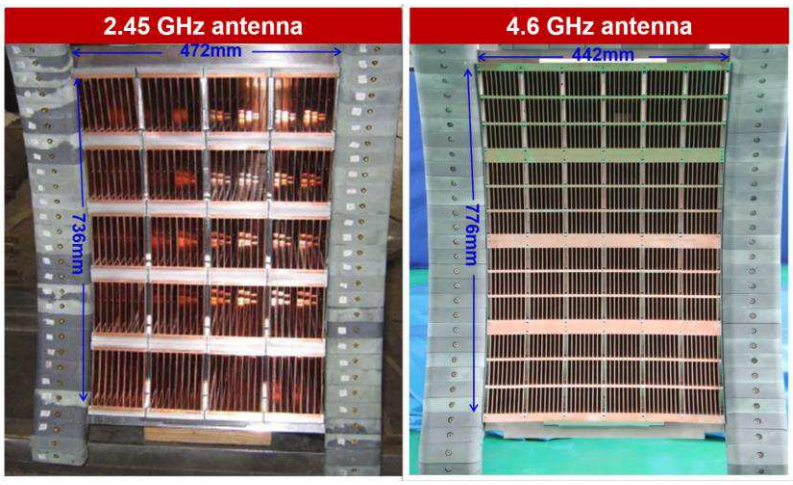

Fig. 1 Front view of 2.45 GHz and 4.6 GHz launchers. The 2.45 GHz launcher arranges in an array of 5 rows and 4 columns, and the 4.6 GHz launcher is in an array of 12 rows and 6 columns.

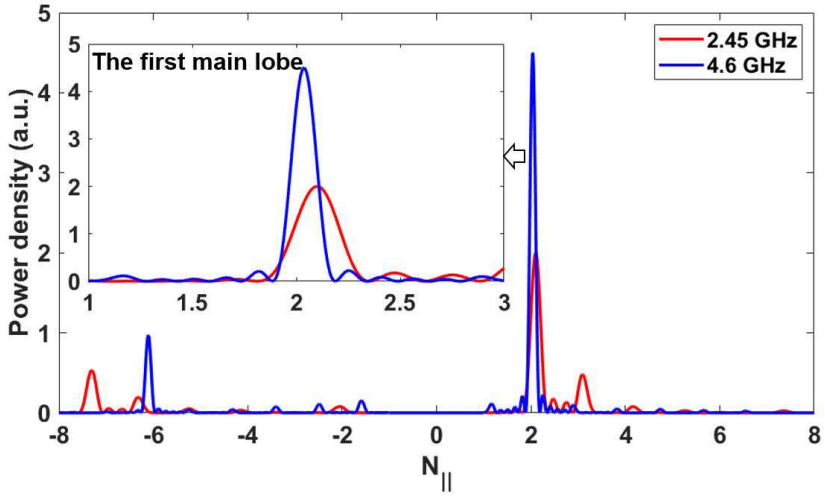

Fig. 2 The launched power spectrum for 2.45 GHz (red) and 4.6 GHz (blue) LH waves. The peak parallel refractive index of the first main lobe is 2.1 (2.45 GHz) and 2.04 (4.6 GHz). The spectral width of the first main lobe ($\Delta N_{||}$) is 0.5 (2.45 GHz) and 0.3 (4.6 GHz).

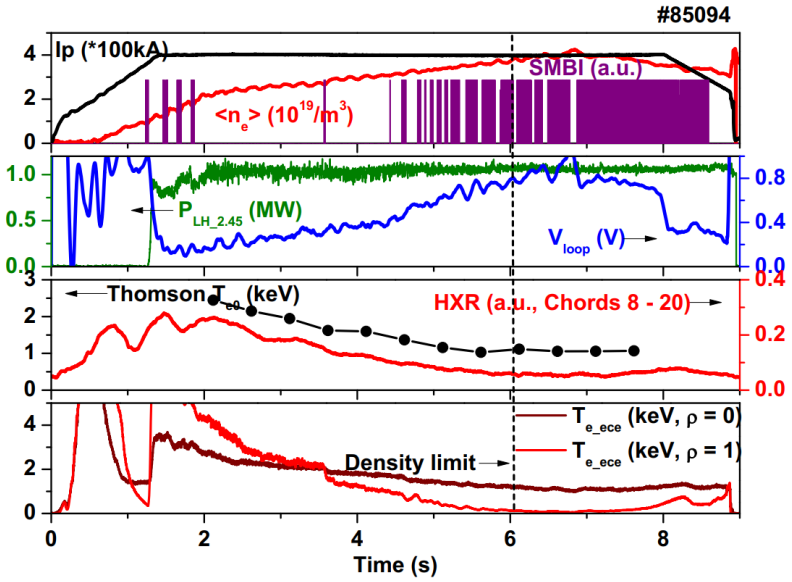

Fig. 3 Typical waveform of density limit experiment with 2.45 GHz LH wave. I_p plasma current; n_e line-averaged density; SMBI supersonic molecular beam injection; $P_{LH_2.45}$ 2.45 GHz LH power; V_{loop} loop voltage; T_{e0} electron temperature at plasma center; HXR hard x radiation; T_{e_ece} electron temperature measured by ECE.

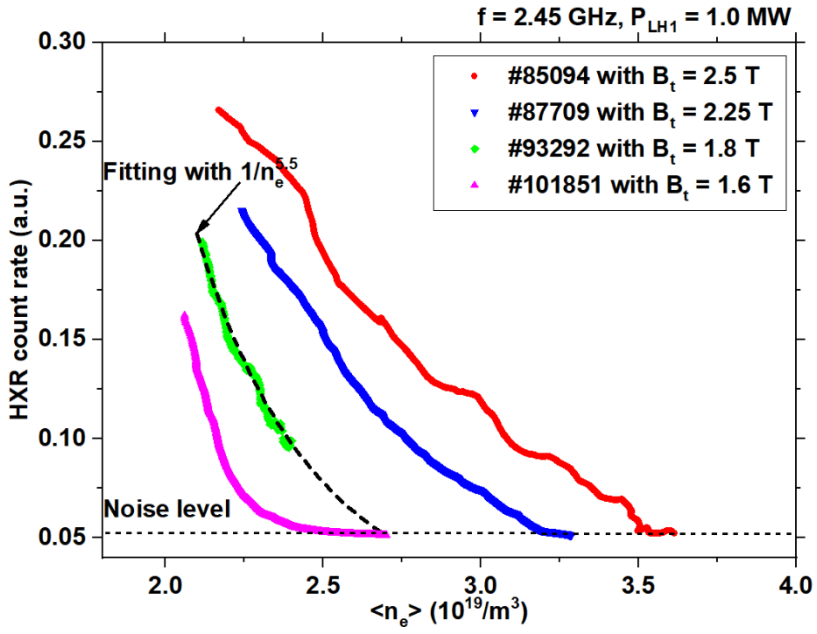

(a)

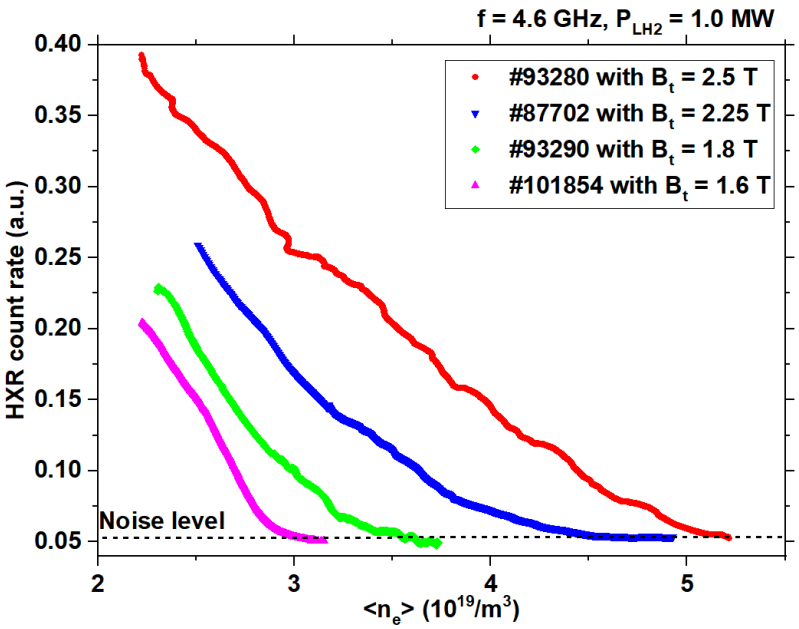

(b)

Fig. 4 Hard X-ray count rates as a function of the line-averaged density with magnetic fields (B_t). (a) for 2.45 GHz and (b) for 4.6 GHz LHCD.

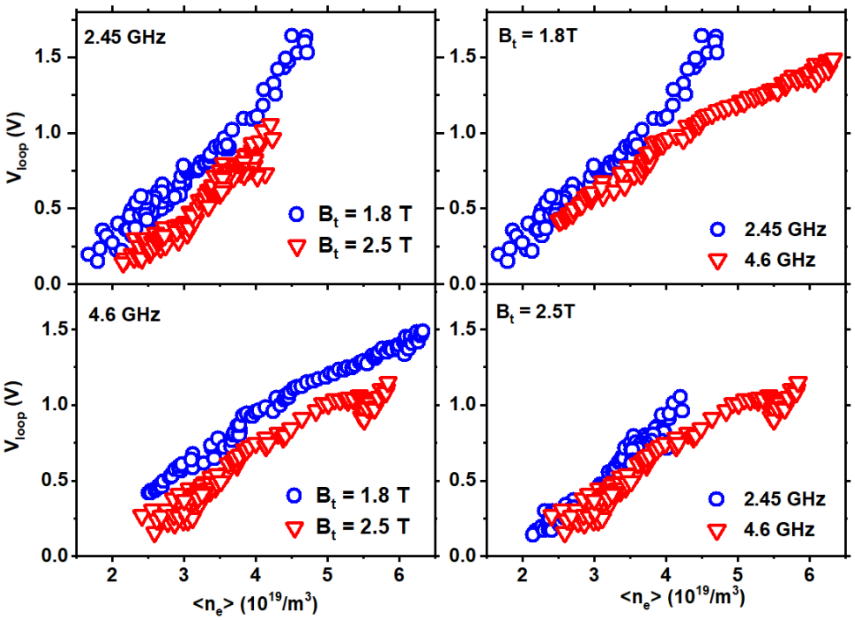

Fig. 5 The residual loop voltage (V_{loop}) as a function of line-averaged plasma density.

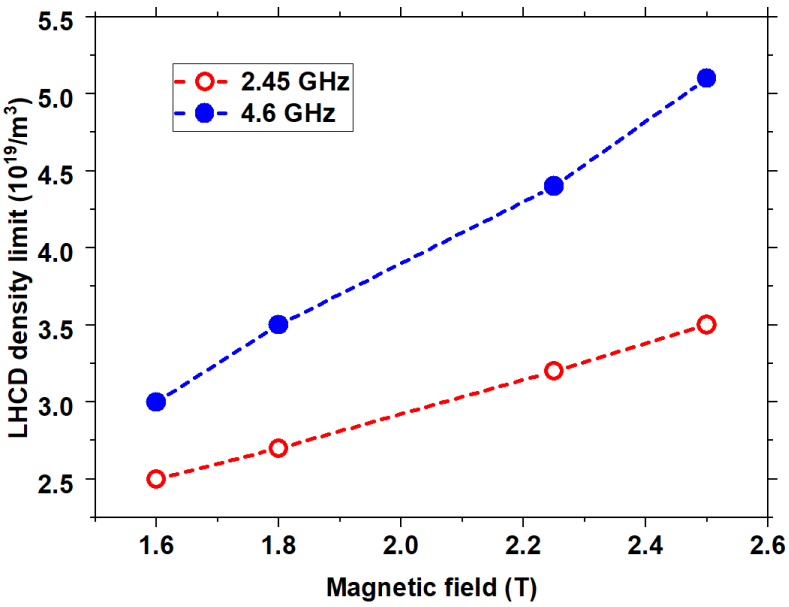

Fig. 6 Observed LHCD density limit (n_{e_limit}) plotted versus the magnetic field for 2.45 GHz (red) and 4.6 GHz (blue) waves respectively.

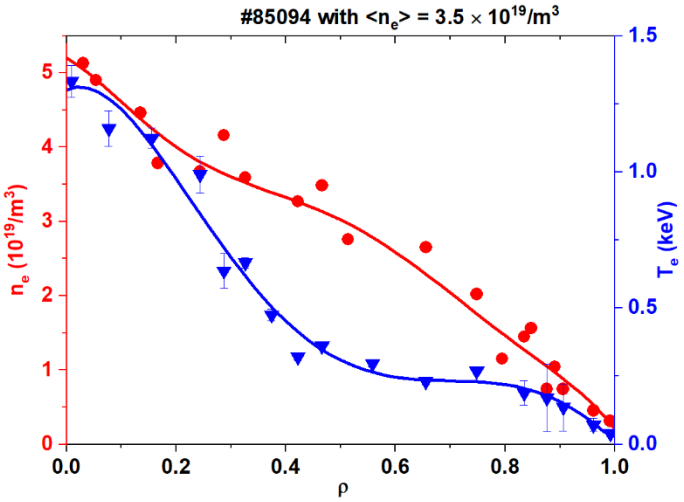

(a)

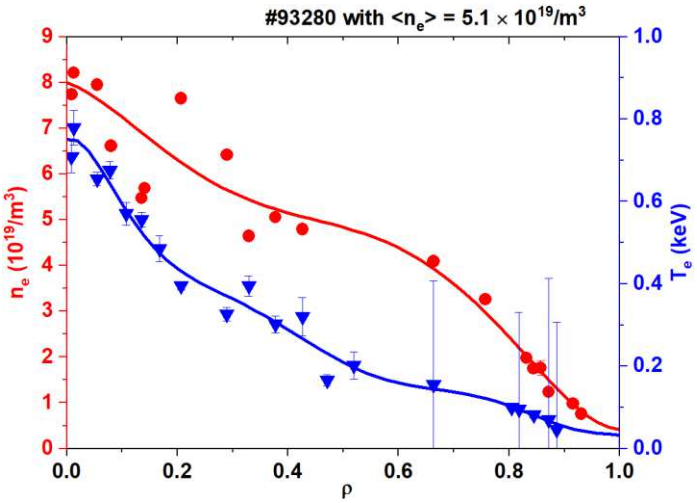

(b)

Fig. 7 Density and temperature profiles used for the ray-tracing simulations which are measured by Thomson scattering. (a) corresponds to the density limit of 2.45 GHz LHCD and (b) corresponds to 4.6 GHz LHCD.

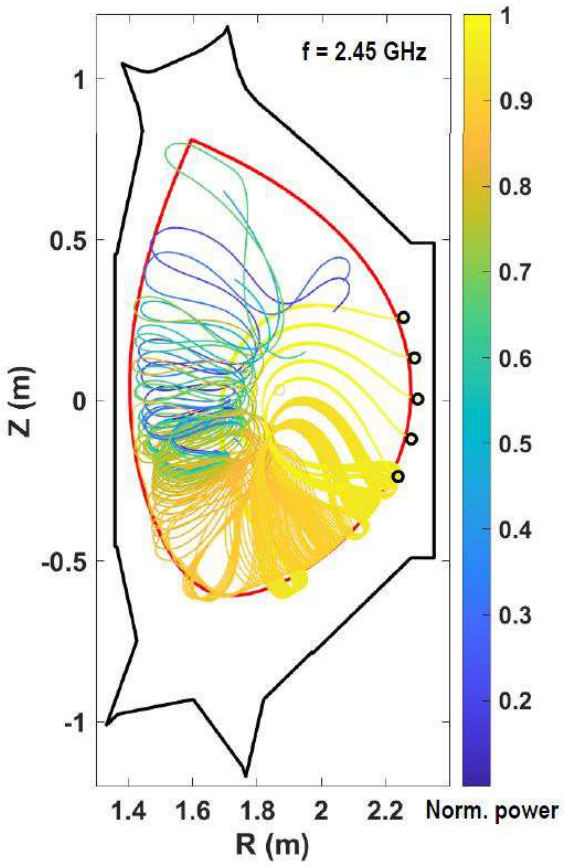

(a)

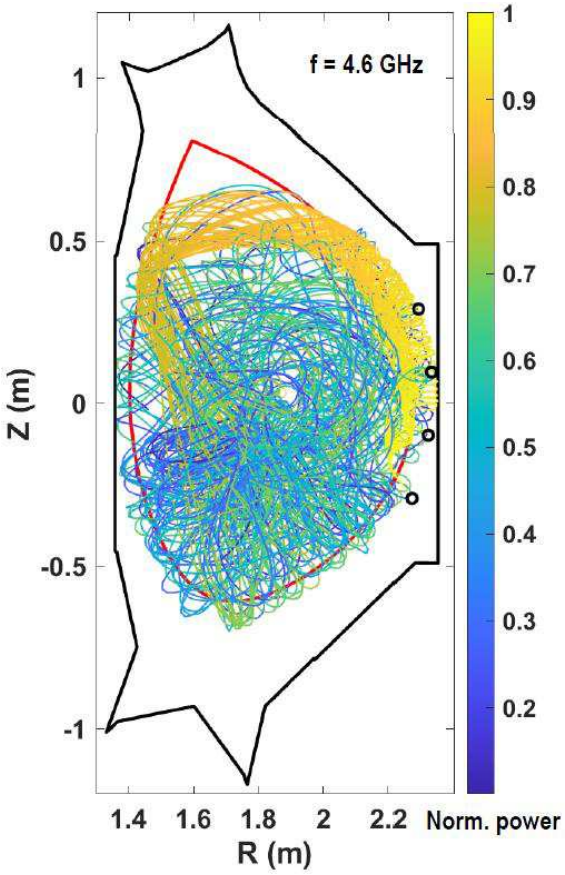

(b)

Fig. 8 Poloidal projections of the ray trajectories calculated with the GENRAY code including propagation in the SOL region. The color-bar denotes the normalized ray power to the initial power. The thick red curve indicates the last closed flux surface and the black circles at the low field side represent the poloidal launching locations.

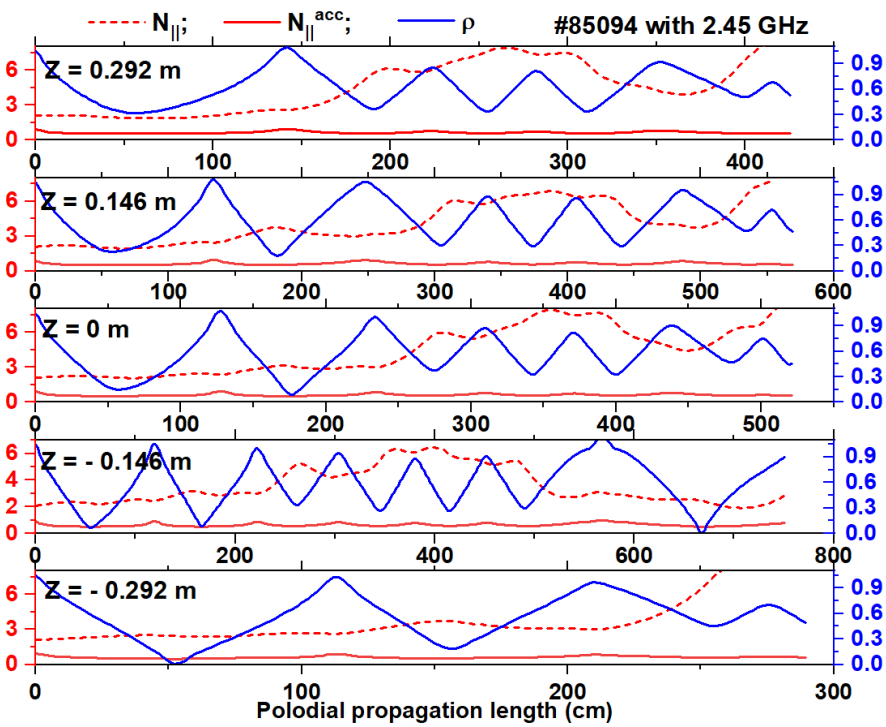

(a)

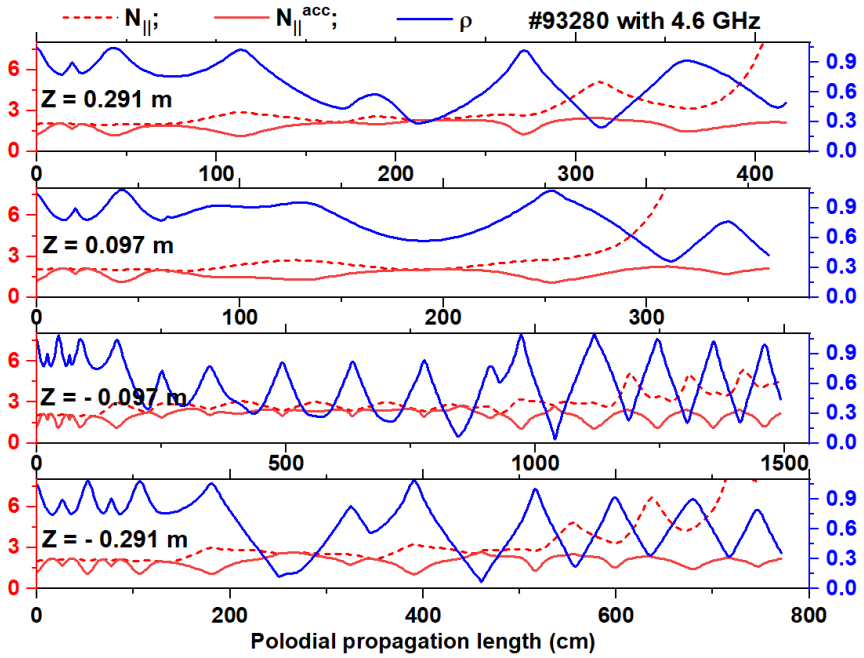

(b)

Fig. 9 The variation of parallel refractive index ($N_{||}$), the local accessibility criterion ($N_{||}^{acc}$), and the normalized radius (ρ) as a function of the poloidal length of ray trajectory. Five poloidal rows of the waveguides are considered for the 2.45 GHz LH wave shown in (a), and four poloidal rows of the waveguides are considered for the 4.6 GHz LH wave shown in (b).

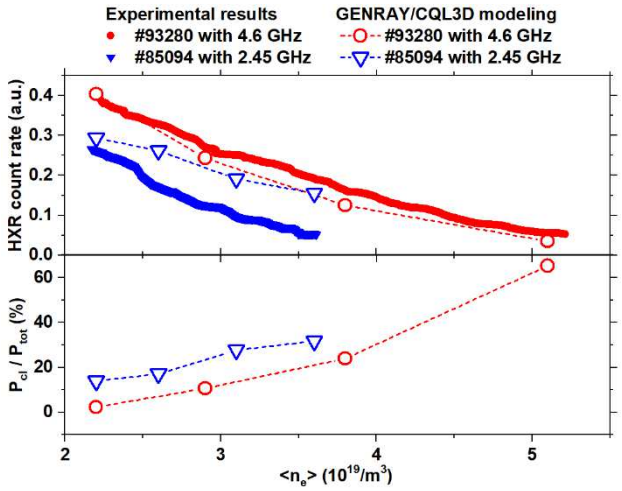

Fig. 10 Comparison of the fast electron bremsstrahlung emission between the experiments and the predictions by GENRAY/CQL3D code package (top panel), and the collisional absorption ratio versus line-averaged density (bottom panel).

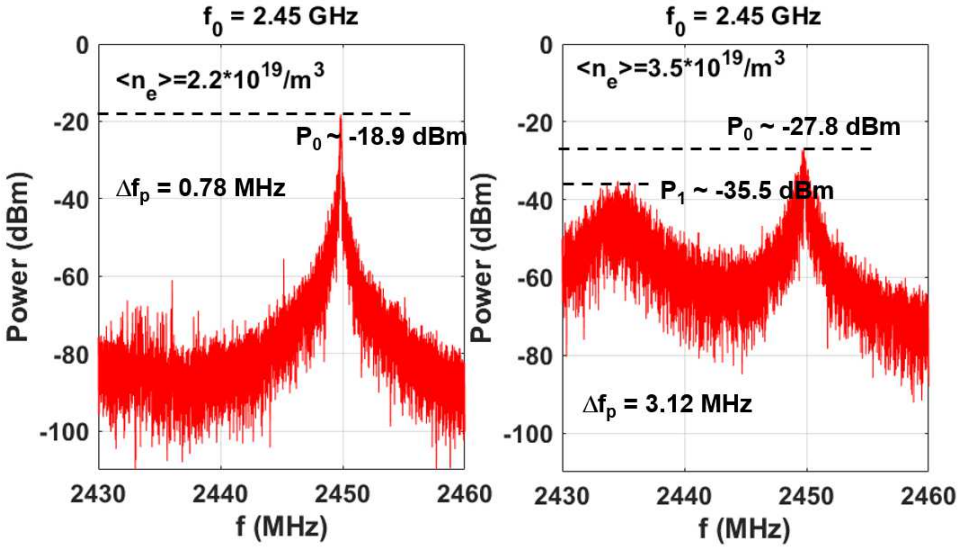

(a)

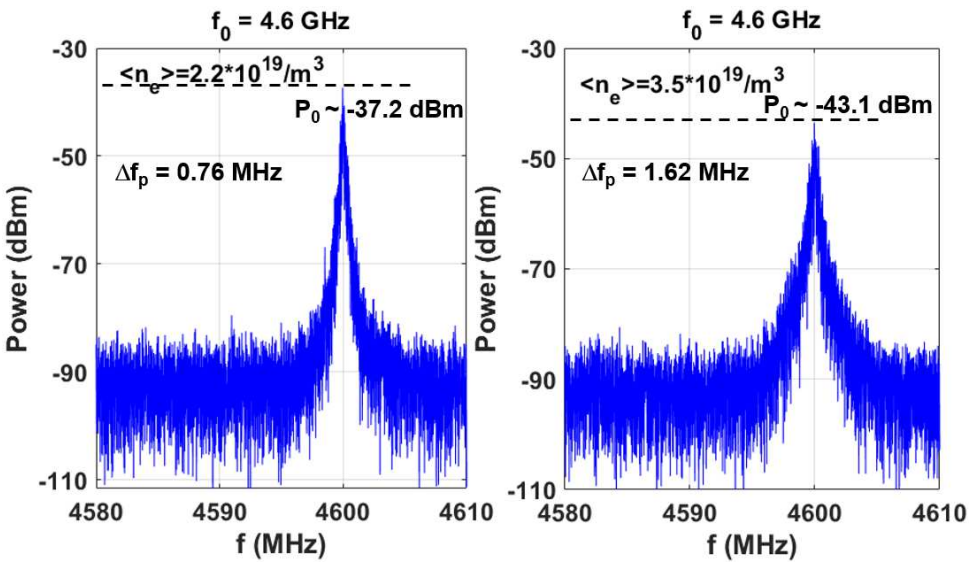

(b)

Fig. 11 Comparison of the frequency spectrum between 2.45 GHz (a) and 4.6 GHz (b) LH waves.

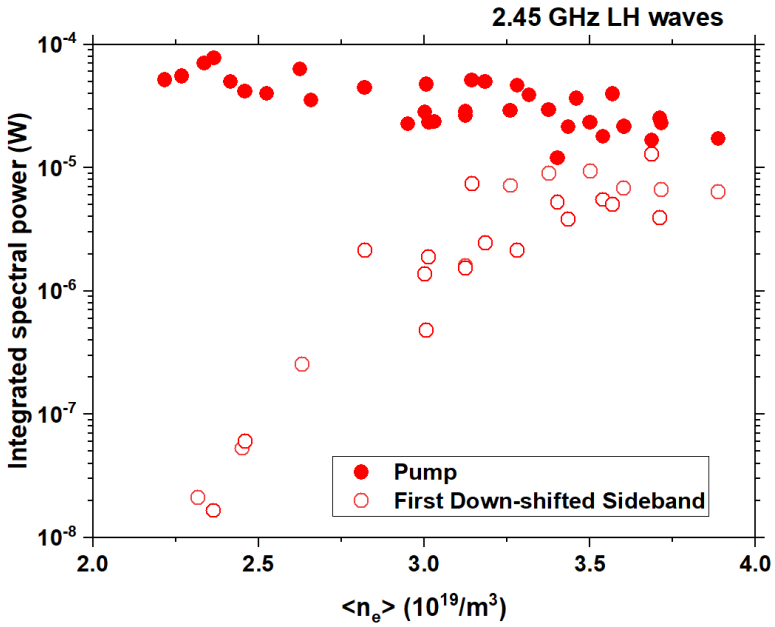

(a)

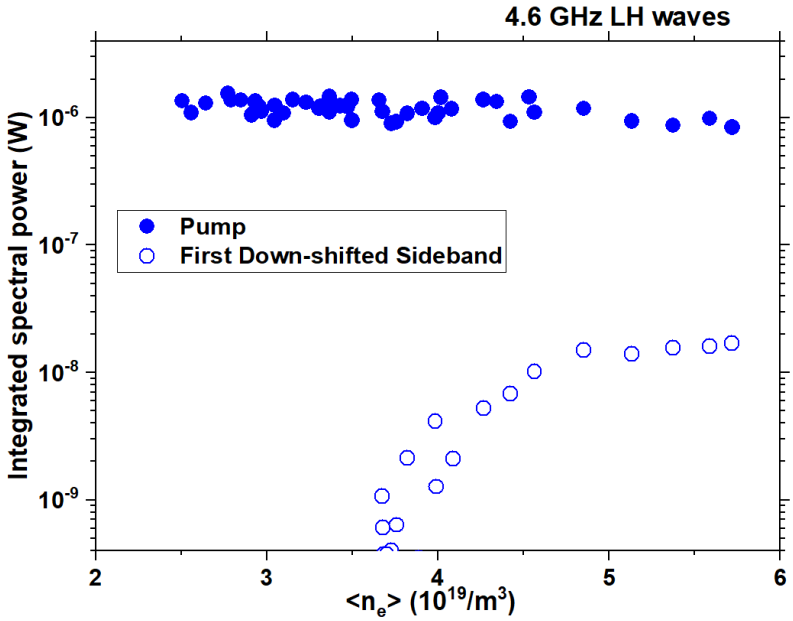

(b)

Fig. 12 Frequency-integrated spectral power of the pump and the first down-shifted sideband. (a) for 2.45 GHz and (b) for 4.6 GHz LH waves.

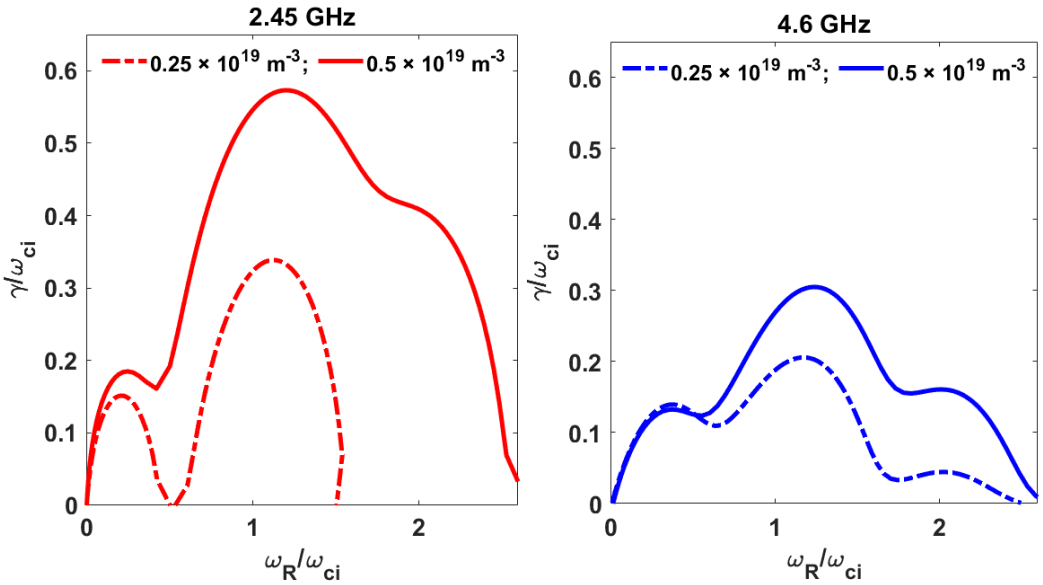

Fig. 13 Growth rate spectra for 2.45 GHz (red) and 4.6 GHz (blue) LH waves with different edge densities.

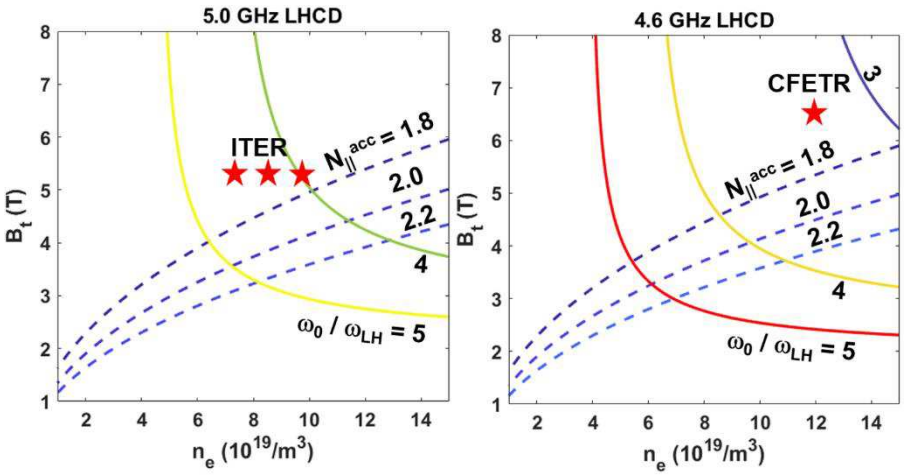

Fig. 14 Wave accessibility ($N_{||}^{acc}$) and parametric decay instabilities (PDIs, indicated by the value of ω_0 / ω_{LH}) assessment for ITER steady-state, inductive and hybrid scenarios and CFETR hybrid scenario. The parameters for ITER scenarios are: $\omega_0 = 2\pi \times 5.0$ GHz, $B_t = 5.3$ T, $n_{e0} = 7.3$ (steady-state), 10.2 (inductive), 8.6 (hybrid) $\times 10^{19}$/m^3. The parameters for CFETR hybrid scenario are: $\omega_0 = 2\pi \times 4.6$ GHz, n_{e0}=12 $\times 10^{19}$/m^3, and $B_t = 6.5$ T.